

## **Cramer-Rao lower bound for support-constrained and pixel-based multi-frame blind deconvolution (Postprint)**

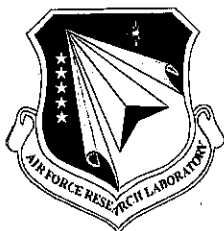
**Charles Matson  
Alim Haji**

**1 September 2006**

**Journal Article**

**APPROVED FOR PUBLIC RELEASE; DISTRIBUTION IS UNLIMITED.**

This is a work of the United States Government and is not subject to copyright protection in the United States.



**AIR FORCE RESEARCH LABORATORY  
Directed Energy Directorate  
3550 Aberdeen Ave SE  
AIR FORCE MATERIEL COMMAND  
KIRTLAND AIR FORCE BASE, NM 87117-5776**

# REPORT DOCUMENTATION PAGE

Form Approved  
OMB No. 0704-0188

Public reporting burden for this collection of information is estimated to average 1 hour per response, including the time for reviewing instructions, searching existing data sources, gathering and maintaining the data needed, and completing and reviewing this collection of information. Send comments regarding this burden estimate or any other aspect of this collection of information, including suggestions for reducing this burden to Department of Defense, Washington Headquarters Services, Directorate for Information Operations and Reports (0704-0188), 1215 Jefferson Davis Highway, Suite 1204, Arlington, VA 22202-4302. Respondents should be aware that notwithstanding any other provision of law, no person shall be subject to any penalty for failing to comply with a collection of information if it does not display a currently valid OMB control number. PLEASE DO NOT RETURN YOUR FORM TO THE ABOVE ADDRESS.

<b>1. REPORT DATE (DD-MM-YYYY)</b> 1 September 2006		<b>2. REPORT TYPE</b> Journal Article (Postprint)		<b>3. DATES COVERED (From - To)</b> Oct 04-Oct 06	
<b>4. TITLE AND SUBTITLE</b> Cramer-Rao lower bounds for support-constrained and Pixel-based multi-frame blind deconvolution (Postprint)				<b>5a. CONTRACT NUMBER</b> F29601-01-D-0083/0006	
				<b>5b. GRANT NUMBER</b>	
				<b>5c. PROGRAM ELEMENT NUMBER</b> 061102F	
<b>6. AUTHOR(S)</b> Charles I. Matson, Alim Haji				<b>5d. PROJECT NUMBER</b> D0D0	
				<b>5e. TASK NUMBER</b> B3	
				<b>5f. WORK UNIT NUMBER</b> AD	
<b>7. PERFORMING ORGANIZATION NAME(S) AND ADDRESS(ES)</b>  AFRL/DESA 3550 Aberdeen Ave. SE Kirtland AFB, NM 87117-5776				<b>8. PERFORMING ORGANIZATION REPORT NUMBER</b>	
<b>9. SPONSORING / MONITORING AGENCY NAME(S) AND ADDRESS(ES)</b>  AIR FORCE RESEARCH LABORATORY 3550 Aberdeen Ave. SE Kirtland AFB, NM 87717-5776				<b>10. SPONSOR/MONITOR'S ACRONYM(S)</b> AFRL/DESA	
				<b>11. SPONSOR/MONITOR'S REPORT NUMBER(S)</b> AFRL-DE-PS-TP-2006-1021	
<b>12. DISTRIBUTION / AVAILABILITY STATEMENT</b>  Approved for Public Release; Distribution is Unlimited.					
<b>13. SUPPLEMENTARY NOTES</b> Author final manuscript published in J. Opt. Soc. Am. A/ Vol. 23, NO. 11, November 2006. This is a work of the United States Government and is not subject to copyright protection in the United States.					
<b>14. ABSTRACT</b> Multi-frame blind deconvolution (MFBD) algorithms can be used to reconstruct a single high-resolution image of an object from one or more measurement frames of that are blurred and noisy realizations of that object. The blind nature of MFBD algorithms permits the reconstruction process to proceed without having separate measurements or knowledge of the blurring functions in each of the measurement frames. This is accomplished by estimating the object common to all the measurement frames jointly with the blurring functions that are different from frame to frame. An issue of key importance is understanding how accurately the object pixel intensities can be estimated with the use of MFBD algorithms. Here we present algorithm-independent lower bounds to the variances of estimates of the object pixel intensities to quantify the accuracy of these estimates when the blurring functions are estimated pixel by pixel. We employ support constraints on both object and the blurring functions to aid in making the inverse problem unique. The lower bounds are presented as a function of the sizes and shapes of these support regions and the number of measurement frames.					
<b>15. SUBJECT TERMS</b> Support, blind deconvolution, multi-frame blind deconvolution, Cramer-Rao lower bounds, image reconstruction, noise reduction.					
<b>16. SECURITY CLASSIFICATION OF:</b>			<b>17. LIMITATION OF ABSTRACT</b>  SAR	<b>18. NUMBER OF PAGES</b>  12	<b>19a. NAME OF RESPONSIBLE PERSON</b> Charles Matson
<b>a. REPORT</b> Unclassified	<b>b. ABSTRACT</b> Unclassified	<b>c. THIS PAGE</b> Unclassified			<b>19b. TELEPHONE NUMBER (include area code)</b> N/A

# Cramér-Rao lower bounds for support-constrained and pixel-based multi-frame blind deconvolution

CLEARED  
FOR PUBLIC RELEASE  
AFRL/DEO-PA  
15E006

Charles L. Matson and Alim Haji

Optics Division, AFRL/DES, Directed Energy Directorate

U.S. Air Force Research Laboratory, 3550 Aberdeen Ave SE, Kirtland AFB, NM 87117-5776 USA

## ABSTRACT

Multi-frame blind deconvolution (MFBD) algorithms can be used to reconstruct a single high-resolution image of an object from one or more measurement frames of that are blurred and noisy realizations of that object. The blind nature of MFBD algorithms permits the reconstruction process to proceed without having separate measurements or knowledge of the blurring functions in each of the measurement frames. This is accomplished by estimating the object common to all the measurement frames jointly with the blurring functions that are different from frame to frame. An issue of key importance is understanding how accurately the object pixel intensities can be estimated with the use of MFBD algorithms. Here we present algorithm-independent lower bounds to the variances of estimates of the object pixel intensities to quantify the accuracy of these estimates when the blurring functions are estimated pixel by pixel. We employ support constraints on both the object and the blurring functions to aid in making the inverse problem unique. The lower bounds are presented as a function of the sizes and shapes of these support regions and the number of measurement frames.

**Keywords:** support, blind deconvolution, multi-frame blind deconvolution, Cramér-Rao lower bounds, image reconstruction, noise reduction

## 1. INTRODUCTION

A common estimation problem is that of reconstructing a high-resolution image of an object from one or more measurement frames that are blurred and noisy realizations of that object. When the blurring functions for all of the measurement frames are known, it is straightforward to reconstruct a high-resolution image of the object whose resolution is limited only by the noise levels in the image and the bandpass of the imaging system. However, in many cases, the blurring functions are not known a priori, nor are separate measurements of them available. A good example of this situation is astronomical imaging from ground-based sites in the presence of atmospheric turbulence when a wavefront sensor is not present. In such situations, multi-frame blind deconvolution (MFBD) algorithms<sup>1</sup> can be used to jointly estimate both the object common to all the measurement frames and each measurement frame's blurring function. In the course of our previous research efforts, we have discovered that our MFBD algorithm can reconstruct unique estimates of the object and the blurring functions as long as the algorithm is regularized properly, the integrated values of the object and each blurring function are constrained to be constant, and appropriate prior knowledge constraints are placed on the object and blurring function reconstructions. In addition, we have discovered that reconstructions of object intensity values produced by our MFBD algorithm have lower variances than produced by competing methods (such as speckle imaging techniques<sup>2</sup>). We have also discovered that, when comparing results from our MFBD algorithm to the results from another MFBD algorithm, our results have lower variances.

Motivated by these last two discoveries, we have undertaken an analysis of the performance of MFBD algorithms to determine fundamental limits to the accuracy of estimates of object intensity values generated by MFBD algorithms in terms of the variances of these estimates. By fundamental limits, we mean limits that are independent of any particular MFBD algorithm. To this end, we are using Cramér-Rao lower bound (CRB) theory<sup>3</sup> to carry out the analysis. This theory can be used to generate algorithm-independent lower bounds (called CRBs) to the variances of any unbiased estimates of a set of parameters. Often unbiased estimates cannot be obtained and thus only biased estimates can be produced. For example, imaging systems produce low-pass-filtered versions of the scenes they image. Without the higher spatial frequencies, only a low-pass-filtered (thus biased) version of the original scene can be reconstructed. The

AFRL/DEO-PA-391

particular low-pass (that is, regularization) filter used in the reconstruction algorithm determines the bias in the reconstruction. When this is the case, CRB theory can be used to generate algorithm-independent but bias (regularization)-dependent lower bounds to the variances of any biased estimates of a set of parameters.

We began this analysis project by assuming that the blurring functions are known (thus the estimation process is non-blind) and explored how the accuracy of estimates of the object intensity values are affected by the inclusion of a support constraint on the object.<sup>4</sup> We generated CRBs for the non-blind case as a function of the size and shape of the support constraint, the type and amount of noise in the measurements, and the type and amount of regularization. To see how well the non-blind version of our MFB algorithm performs, we then compared sample variances produced using this version of our MFB algorithm to the CRBs and discovered that the sample variances were either the same or close to the CRBs.

In this paper, we present our initial results describing the application of CRB theory to blind deconvolution when both the object and the blurring functions are estimated pixel by pixel in the image domain. We employed support constraints to make the inverse problem (for a given regularization filter) unique. We generated object CRBs (hereafter referred to just as CRBs) as a function of the size and shape of both the object and blurring function support constraints and the number of measurement frames. Herein we present some of these CRBs and compare them to the non-blind case. In general, the pixel-based blind deconvolution CRBs are greater (often by more than an order of magnitude) than the associated non-blind CRBs. The paper is organized as follows: Section 2 contains the imaging model used for the results in this paper, CRB theory is described briefly in Section 3, results are given in Section 4, and conclusions and future work are presented in Section 5.

## 2. PROBLEM FORMULATION

The equation describing image formation is

$$\mathbf{i}(\mathbf{x}) = \mathbf{h}(\mathbf{x}) * \mathbf{o}(\mathbf{x}) + \mathbf{n}(\mathbf{x}) \quad (1)$$

where bold-face type indicates vector or matrix quantities,  $*$  denotes convolution,  $\mathbf{x}$  is a two-dimensional spatial variable,  $\mathbf{i}(\mathbf{x})$  is the measured image,  $\mathbf{h}(\mathbf{x})$  is the system point spread function (PSF),  $\mathbf{o}(\mathbf{x})$  is the object being imaged, and  $\mathbf{n}(\mathbf{x})$  is the zero-mean noise corrupting the measured image. Although  $\mathbf{n}(\mathbf{x})$  is shown as additive, it models both Poisson and CCD read noise. For the results presented in Section 4, we model  $\mathbf{h}(\mathbf{x})$  as being the PSF associated with imaging through the atmosphere using an ideal imaging system with an unobscured aperture. We characterize the imaging system by the diameter  $D$  of its exit pupil and the atmosphere by the Fried parameter  $r_0$ .<sup>2</sup> All the results in Section 4 assume that the ratio  $D/r_0$  is equal to four. The true object used for  $\mathbf{o}(\mathbf{x})$  in Section 4 is the satellite model shown in Fig. 1.

## 3. CRAMÉR-RAO LOWER BOUND THEORY

We first present a brief overview of both unbiased and biased CRB theory in this section. Although only biased CRB theory is used for the results in Section 4 since  $\mathbf{h}(\mathbf{x})$  is a low-pass filter, the unbiased CRB theory provides important insight into how the biased CRBs are generated, both theoretically and numerically. We then discuss numerical implementation issues that undergird the results in Section 4.

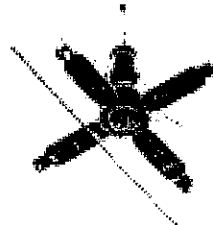


Fig. 1. Computer-simulated satellite model used for CRB results.

### 3.1 Unbiased CRB theory

Standard CRB theory, both unbiased and biased, assumes that the number of parameters to be estimated are finite. For this reason, the imaging model of Eq.(1) must be rewritten in a vector form rather than as a function of the continuous variable  $x$ . To this end, let  $\alpha$  be a vector of length  $N$  that contains the  $N$  spatial locations of the intensity values of  $i(x)$  as would be obtained for an image collected with a CCD array. Then let  $y$ ,  $\theta$ , and  $\eta$  be one-dimensional vectors that contain the values of  $i(\alpha)$ ,  $o(\alpha)$ , and  $n(\alpha)$ , respectively, on the grid defined by  $\alpha$ . In addition, let  $H$  be the block-circulant system matrix associated with  $h(\alpha)$ .<sup>5</sup> This permits rewriting Eq.(1) as a matrix-vector equation given by

$$y = H\theta + \eta. \quad (2)$$

and the PDF of  $\eta$  is denoted by  $f_\eta(\eta)$ . In blind deconvolution, the functionally-independent parameters that generate the elements of both  $H$  and  $\theta$  are estimated. Let  $\Phi$  be a vector that contains all of these parameters. For pixel-based estimation of  $h(\alpha)$  and  $o(\alpha)$  when  $\sum_{n=1}^N o(\alpha_n)$  and  $\sum_{n=1}^N h(\alpha_n)$  are both fixed quantities, only  $N-1$  elements of both  $h(\alpha)$  and  $o(\alpha)$  are functionally independent. Without loss of generality, we assume that the first  $N-1$  elements of both  $h(\alpha)$  and  $o(\alpha)$  are used to generate  $H$  and  $\theta$  and thus are the elements of the vector  $\Phi$ . The CRBs for any unbiased estimate of the elements of  $\Phi$  are the diagonal elements of the inverse of the Fisher information matrix,  $F$ , associated with  $y$ ,  $\Phi$ , and  $\eta$ . Therefore, we next define  $F$ . Let  $f(y; \Phi)$  be the PDF of  $y$  parameterized by the vector  $\Phi$ . Then the element of  $F$  in the  $p^{\text{th}}$  row and the  $q^{\text{th}}$  column is given by

$$F_{pq} = E \left[ \frac{\partial \ln f(y; \Phi)}{\partial \Phi_p} \frac{\partial \ln f(y; \Phi)}{\partial \Phi_q} \right] \quad (3)$$

where  $E[\cdot]$  denotes the expected value of the quantity in the brackets,  $\ln$  denotes the natural logarithm and  $\Phi_p$  denotes the  $p^{\text{th}}$  element of  $\Phi$ . From Eq.(2), it follows that

$$f(y; \Phi) = f_\eta(y - H\theta) \quad (4)$$

where the notation  $f_\eta(y - H\theta)$  denotes  $f_\eta(\eta)$  with  $\eta$  replaced by  $y - H\theta$ . For Poisson and CCD read noise, an excellent approximation to  $F_{pq}$  is given by<sup>6</sup>

$$F_{pq} = \sum_k \left\{ \frac{\partial (H\theta)_k}{\partial \Phi_p} \frac{\partial (H\theta)_k}{\partial \Phi_q} \left[ (H\theta)_k + \sigma^2(\alpha_k) \right]^{-1} \right\} \quad (5)$$

where the summation is over all the elements of  $\alpha$ ;  $(H\theta)_k$ ,  $\theta_k$ , and  $\alpha_k$  are the  $k^{\text{th}}$  elements of  $H\theta$ ,  $\theta$ , and  $\alpha$ , respectively; and  $\sigma^2(\alpha_k)$  is the spatially-dependent CCD read noise variance. For either type of noise by itself (i.e., when either  $(H\theta)_k$  or  $\sigma^2(\alpha_k)$  is zero in the last factor in Eq.(5)), the corresponding expression for  $F_{pq}$  is exact. The form of  $F_{pq}$  is a summation over all the pixel locations because both Poisson and CCD read noises are spatially independent and thus the joint pdf of the noise for all pixels is just the multiplication of the single-pixel pdfs, and the natural logarithm operation converts the multiplication to a summation.

Equation (5) gives the elements of  $F$  for the imaging model of Eq.(2) without the application of any constraints. A support constraint can be implemented easily by including in the vector  $\Phi$  only the values of  $o(\alpha)$  and  $h(\alpha)$  for which  $\alpha$  is in the known support regions of  $o(\alpha)$  and  $h(\alpha)$ , respectively.<sup>7</sup>

The equations above are valid for a single measurement frame but can be extended easily to accommodate multiple measurement frames. To do so, assume that there are  $M$  measurements to be used to jointly estimate the pixel intensities of a single object and  $M$  PSFs. First, create  $M$  measurement vectors separately as described above and then stack them to create a single composite column vector that has  $MN$  elements. The composite noise vector is created in the same way. The composite system matrix  $H$  is created by stacking the individual system matrices in a block-column

manner so that it has dimensions of  $MN$  by  $N$ . The object vector  $\theta$  is the same for single or multiple measurement frames since it is assumed to be the same for all the measurements. Finally, the composite parameter vector  $\Phi$  contains all the functionally-independent object and PSF parameters for all the measurements and thus has  $(M+1)(N-1)$  elements when there are no support constraints. The elements in  $\Phi$  can be placed in any desired order. When support constraints are placed on  $o(\alpha)$  and  $h(\alpha)$ , the number of elements in  $\Phi$  is reduced accordingly.

### 3.2 Biased CRB theory

The standard approach to biased CRB theory is to generate the biased CRBs in terms of the inverse of  $F$  and the gradient of the bias with respect to the parameters. Mathematically, let  $b(\Phi)$  be the bias of an estimate of  $\Phi$  and let  $\nabla_{\Phi} b$  be its gradient with respect to  $\Phi$ . Then the CRBs of any estimator with bias  $b(\Phi)$ ,  $BCRB_{\Phi}$ , are given by

$$BCRB_{\Phi} = \text{diag}[(\nabla_{\Phi} b) F^{-1} (\nabla_{\Phi} b)^T] \quad (6)$$

where  $\text{diag}[\cdot]$  denotes the diagonal elements of the matrix in the brackets. Equation (6) assumes that  $F$  is invertible. When it is not invertible, its inverse is replaced by its pseudo-inverse,  $F^+$ , with the requirement that the range space of  $(\nabla_{\Phi} b)^T$  is contained in the orthogonal complement of the null space of  $F^+$ . In terms of our imaging model, this requirement can be stated equivalently as that any regularization filter must have a bandpass contained within the bandpass of the imaging system.

When a support constraint is applied to the imaging model of Eq.(1), the forward model is invertible but its inverse is discontinuous. This fact, applied to the discrete form of the imaging model (Eq.(2)) and  $F$  (Eq.(5)), means that  $F$  is invertible but highly ill-conditioned. For this reason, the standard pseudo-inverse approach to generating an inverse of  $F$  is highly sensitive to the numerical level at which the eigenvalues of  $F$  are deemed to be at or below the numerical precision of the computer. We have tried various schemes for determining the best eigenvalue cutoff as well as methods other than truncation for inclusion or exclusion of eigenvalues in the pseudo-inverse calculations, but have not been able to mitigate the sensitivities of the CRB values to the particular pseudo-inversion scheme employed. For this reason, we have been exploring alternate ways to generate biased CRBs using a modified version of Eq.(6).

In the known PSF case when the PSF is not invertible and a support constraint is applied, we were able to fully ameliorate the pseudo-inverse problems<sup>8</sup> by adding to the known PSF a second PSF that is the inverse Fourier transform of an ideal high-pass filter that is zero where the Fourier transform of the known PSF is non-zero and is a small constant everywhere else. The sum of the known and high-pass-filter PSFs is invertible, permitting  $F^{-1}$  to be calculated. Furthermore, when the bandpass of the regularization filter is contained within the bandpass of the imaging system, the contributions of the high-pass-filter PSF to  $F^{-1}$  are all contained in the orthogonal complement to the range space of  $(\nabla_{\Phi} b)^T$ . This means that the biased CRBs calculated using Eq.(6) depend only on the system PSF and not the high-pass-filter PSF. For blind deconvolution, unfortunately, this approach does not work because the PSF pixel values are jointly estimated with the object pixel values.

For the CRBs in the next section, we apply a support constraint on the system PSF as well as on the object to render  $F$  invertible for use in Eq.(6). Because the system PSF is bandlimited, it does not have finite support; however, for large enough support sizes, most of the energy is contained in the support region and thus hopefully will have minimal impact on the CRBs. In Section 4, we will show the impact of the PSF support size on the CRBs.

## 4. RESULTS

We present biased CRB results for pixel-based blind deconvolution in this section for a variety of scenarios. For all the results, the object in Fig. 1 was used to create  $\theta$ . For the case of  $M$  measurement frames, where  $M$  is arbitrary, the system matrix  $H$  was created using the  $M$  system PSFs that were used to generate the measurement frames. Each system PSF was created using a Fourier-optics model for incoherent imaging<sup>9</sup> assuming an ideal imaging system with the addition of phase distortions in its pupil (of diameter  $D$ ) brought about by atmospheric turbulence characterized by  $D/r_0 = 4$ . The phase distortions from PSF to PSF are statistically independent.

Using the object and system PSFs described above, we calculated blind CRBs for various combinations of three different support constraints on the object and two different support constraints on the system PSF. For all cases, the noise was modeled as white, zero-mean Gaussian noise with a variance of 100. The three object supports constraints

are shown in Fig. 2. The first is the true object support, the second is a blurred version of the true object support, and the third is the smallest centered circle that contains the true object. Both PSF support constraints are circular regions centered on the origin. The first has a diameter that is 33% of the array width and the second has a diameter that is 64% of the array width. Results will be shown in this section for a subset of these parameter sets. In addition, we will compare the blind CRBs to the corresponding non-blind CRBs. All CRBs, both blind and non-blind, were calculated assuming that the object was regularized using an ideal low-pass filter whose cutoff frequency was just inside the cutoff frequency of the imaging system.

The results corresponding to using the true object support and the 33% circular PSF support as constraints are shown in Figs. 3 and 4. In Fig. 3, two-dimensional scaled displays are shown of the CRBs for the non-blind case, for the blind case with one measurement frame, and for the blind case with ten measurement frames. It can be seen that the non-blind CRBs increase as the distance from the edge of the object support region increases. The reason for this behavior has been discussed previously.<sup>4,8</sup> The spatial structure of the blind CRBs is more complicated than for the non-blind case and we are not entirely sure at this time why the structure is the shape that it is. Notice that the spatial structure is essentially the same for the one and ten measurement frame cases.

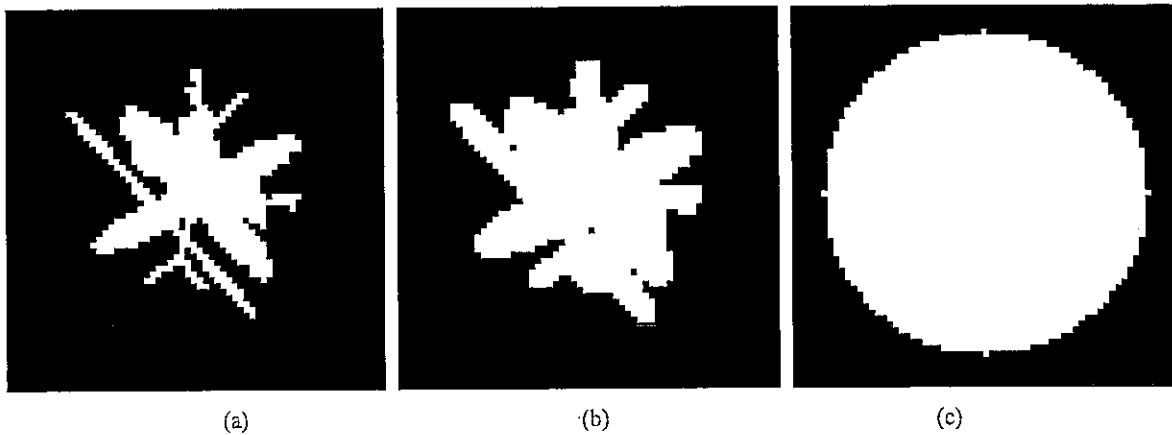


Fig. 2. Object support constraints used in the blind and non-blind CRB calculations: (a) true support, (2) blurred support, and (c) circular support.

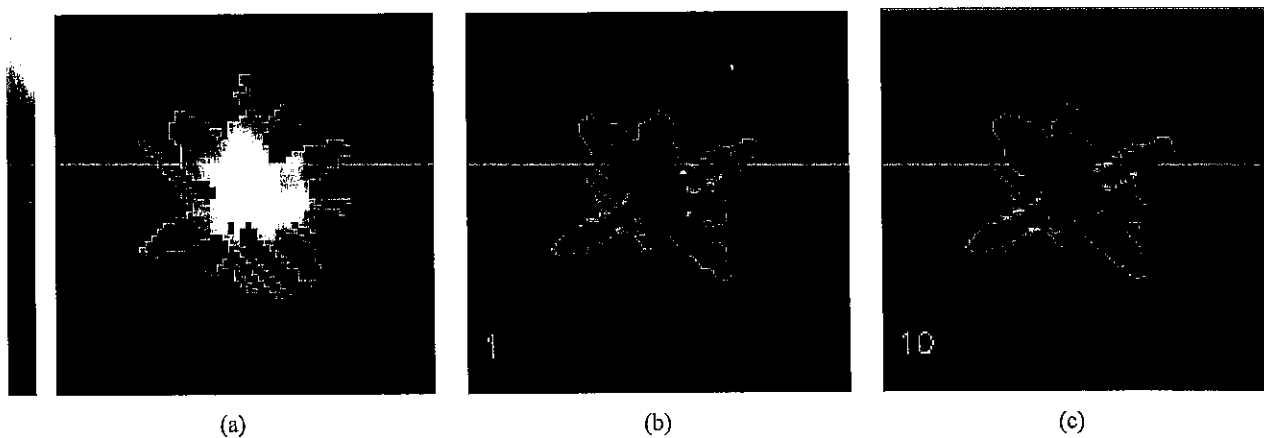


Fig. 3. Scaled CRBs when using the true object support and the 33% circular PSF support as constraints: (a) non-blind case, (b) blind case for one measurement frame, and (c) blind case for ten measurement frames. The CRB maps are scaled to their minimum and maximum values. The minimum and maximum CRB values are indicated by black and yellow, respectively, and intermediate CRB values are mapped to colors according to the color bar to the left of the figure.

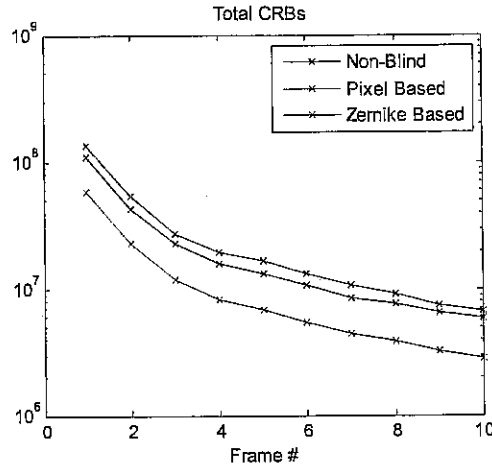


Fig. 4. Totals of the unscaled CRBs corresponding to Fig. 3 as a function of the number of measurement frames used in the estimation process.

The totals of the unscaled CRBs for an object estimate (that is, the sum of all the unscaled single-pixel CRBs) corresponding to Fig. 3 are plotted in Fig. 4 as a function of the number of measurement frames used in the estimation process. Notice that both the non-blind and blind CRBs decrease at approximately the same rate as a function of the number of frames. Notice also that, although the blind CRBs are higher than the non-blind CRBs, they are still relatively similar in magnitude.

The results corresponding to using the true object support and the 64% circular PSF support as constraints are shown in Figs. 5 and 6. These results are for the same scenario as the results in Figs. 3 and 4 with the exception that the area of the PSF support is approximately four times larger in Figs. 5 and 6. By comparing Fig. 3 with Fig. 5, it can be seen that there is a little difference in the spatial structure of the blind CRBs, but not much. More importantly, it can be seen by comparing Fig. 4 with Fig. 6 that the totals of the blind CRBs have increased by a factor of four. Clearly, the size of the PSF support constraint plays a big role in the CRB totals.

The results corresponding to using the blurred object support and the 33% circular PSF support as constraints are shown in Figs. 7 and 8. Notice that the spatial structure of the blind CRBs in Fig. 7 shows that the blind CRBs are much higher at the edges of the true object support than anywhere else in the blurred object support. This is an interesting result because the non-blind CRBs are known to always be lowest at the edges of the enforced support region for the white noise case considered here due to noise correlation effects, regardless of the true object support.<sup>4,8</sup> The blind CRBs in

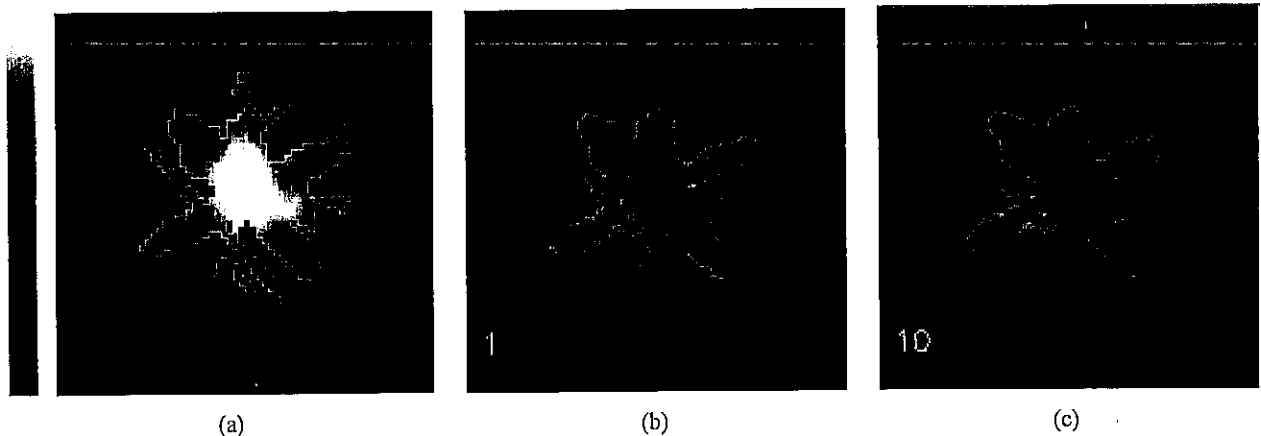


Fig. 5. Scaled CRBs when using the true object support and the 64% circular PSF support as constraints: (a) non-blind case, (b) blind case for one measurement frame, and (c) blind case for ten measurement frames.



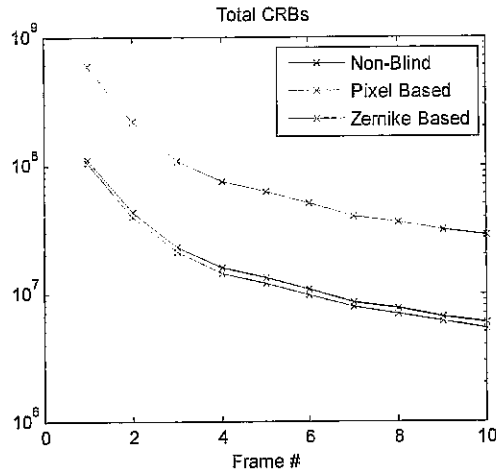


Fig. 6. Totals of the unscaled CRBs corresponding to Fig. 5 as a function of the number of measurement frames used in the estimation process.

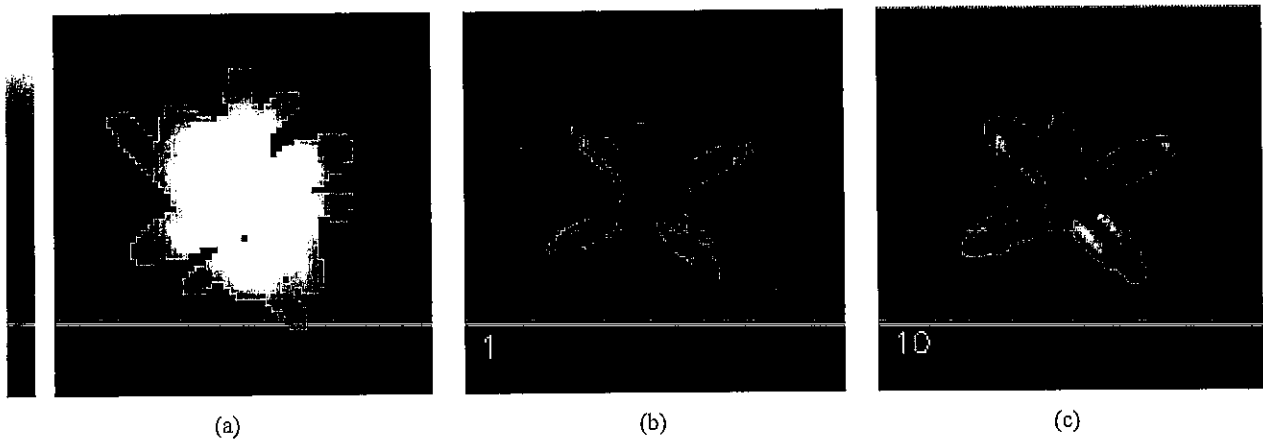


Fig. 7. Scaled CRBs when using the blurred object support and the 33% circular PSF support as constraints: (a) non-blind case, (b) blind case for one measurement frame, and (c) blind case for ten measurement frames.

Fig. 7 are indicating that, when the PSF must be jointly estimated with the object, and the object support constraint is not known precisely, the edges of the object are more difficult to estimate than the interior regions. The edges correspond to high spatial frequencies, so the results in Fig. 7 imply that the higher spatial frequencies of the object are more difficult to estimate when jointly estimating the object and PSF pixel values. By comparing the blind CRBs for one and ten measurement frames, it can be seen that the addition of more measurement frames reduces the CRBs of the object pixel value estimates at the edges of the true object support more than in the interior. This is indicated in Fig. 7 by the fact that the CRBs interior to the true object support are a higher percentage of the CRBs at the edges of the true object support than for the one measurement frame case, keeping in mind that each two-dimensional display of the CRBs is scaled to the maximum value in each display.

Plots of the totals of the blind and non-blind CRBs as a function of the number of measurement frames corresponding to the CRBs in Fig. 7 are shown in Fig. 8. Notice that both the blind and non-blind CRBs are larger than the corresponding results in Fig. 4 because of the less-accurate object support constraint. In addition, notice that the blind CRB for one measurement frame is approximately a factor of ten larger than when the perfect object support is used as a constraint, while the corresponding factor for the non-blind case is approximately a factor of two larger. This implies that blind deconvolution is more sensitive to the accuracy of the support constraints than is non-blind deconvolution. Finally, notice the large decrease (a factor of five) in the blind CRBs when two instead of one measurement frames are used. This behavior is one we have noticed when using our blind deconvolution algorithm on real data – the results

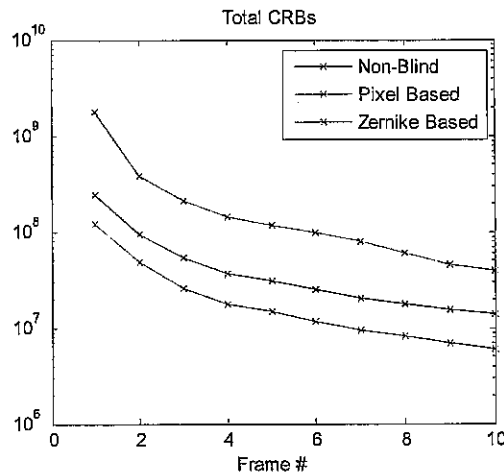


Fig. 8. Totals of the unscaled CRBs corresponding to Fig. 7 as a function of the number of measurement frames used in the estimation process.

from including two or three measurement frames in the estimation process are much less noisy than when including just one measurement frame.

The final results to be presented are shown in Figs. 9 and 10 for the case of using a circular object support constraint and the 33% circular PSF support constraint. The conclusions to be drawn from these figures are qualitatively the same as those drawn from Figs. 7 and 8. As before, the spatial structure of the non-blind CRBs are a function of the applied object support constraint, not the true object support region. The spatial structure of the blind CRBs is a function of the true object support, not the applied object support, and are higher at the edges of the true object support. In addition, the blind CRBs at the edges of the true object support decrease faster as more measurement frames are added than do the blind CRBs interior to the true object support. We see a large decrease in the blind CRBs when including two instead of one measurement frames in the estimation process as was the case when applying the blurred object support; however, the decrease is a factor of sixty instead of only a factor of five. This means that including more measurement frames in a blind deconvolution algorithm is much more important when the applied object support constraint is less accurate than when the applied object support constraint is more accurate.

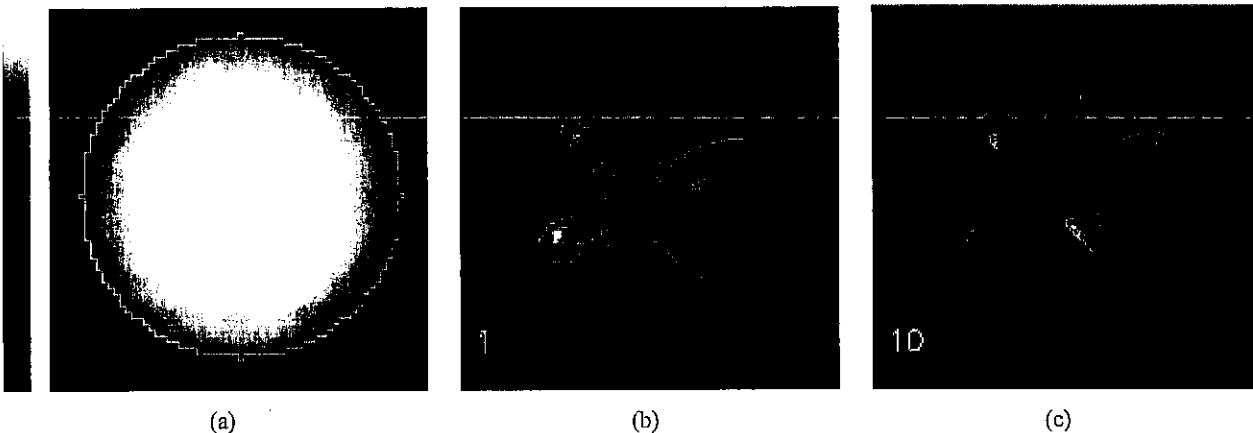


Fig. 9. Scaled CRBs when using the circular object support and the 33% circular PSF support as constraints: (a) non-blind case, (b) blind case for one measurement frame, and (c) blind case for ten measurement frames.

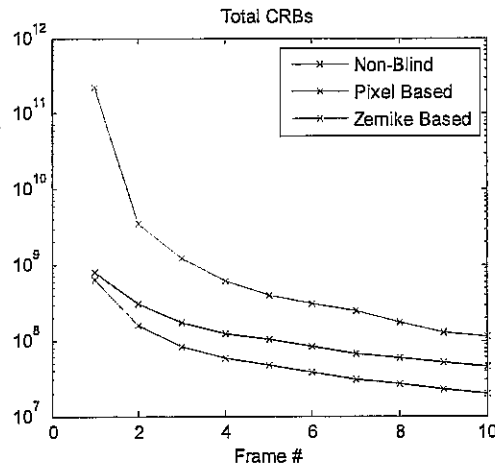


Fig. 10. Totals of the unscaled CRBs corresponding to Fig. 9 as a function of the number of measurement frames used in the estimation process.

## 5. CONCLUSIONS AND FUTURE WORK

We have presented CRBs for blind deconvolution in this paper and compared them to the corresponding non-blind CRBs. The CRBs were generated assuming that the measurements consisted of the sum of a true object blurred by atmospheric turbulence and white Gaussian noise. It was further assumed that the information incorporated in the blind estimation process included both object and PSF support constraints; obviously, no PSF support constraint is needed for the non-blind case. We showed that the blind CRBs are always larger than the non-blind CRBs – an expected result since more parameters are estimated in the blind case. We also showed that, although both blind and non-blind CRBs increase as the size of the applied object support constraint increases, the blind CRBs increase much faster than the non-blind CRBs.

There are several properties of the blind CRBs that are unique to blind deconvolution. The first is that a PSF support constraint is needed and the blind CRBs are an increasing function of the size of this support. We have included a PSF support constraint in order to make the Fisher information matrix invertible for non-invertible PSFs due to the way that the biased CRBs are calculated. A PSF support constraint generates a bias in the CRBs in addition to the bias produced by regularization. As the PSF support size increases, the bias decreases with a concomitant increase in variance. In future work we plan to revisit how we calculate biased CRBs to remove this aspect of bias from their values. We note, however, our initial investigations of bias versus variance in the context of PSF support constraints indicates that there is a large decrease in variance for a small increase in bias; therefore, it may be appropriate to always include PSF support constraints.

The second property we wish to mention is that the spatial structure of blind CRBs is a function of the true object support, not the applied object support, unlike for the non-blind CRBs. In particular, the edges of an object are harder to estimate accurately than is the interior of an object. Because edges are important cues for the human visual system, this is a severe drawback of pixel-based blind deconvolution algorithms.

In the future, we plan to extend this work to blind deconvolution algorithms where the PSF is parameterized by a modal decomposition of the phase in the imaging system exit pupil. Our experience, and the experience of others, is that blind object reconstruction with this parameterization of the PSFs is much more accurate than pixel-based blind deconvolution.

## ACKNOWLEDGEMENTS

The authors thank the Air Force Office of Scientific Research and the Air Force Research Laboratory for their financial support that made this research possible. They also thank Dr. Sudhakar Prasad and Mr. Chip Beckner for many helpful discussions.

## REFERENCES

- <sup>1</sup> D. Kundur and D. Hatzinakos, "Blind image deconvolution," *IEEE Signal Processing Magazine*, 43-63 (May 1996).
- <sup>2</sup> M. C. Roggemann and B. Welsh, *Imaging Through Turbulence*, CRC Press, Boca Raton (1996).
- <sup>3</sup> B. Porat, *Digital Processing of Random Signals -Theory and Methods*, Ch. 3, Prentice-Hall, Englewood Cliffs (1994).
- <sup>4</sup> C. L. Matson, C. C. Beckner, and K. J. Schulze, "Fundamental limits to noise reduction in images using support: benefits from deconvolution," in Image Reconstruction from Incomplete Data III, P. J. Bones, M. A. Fiddy, and R. P. Millane, eds., *Proceedings of the SPIE* 5562, 161-168 (2004).
- <sup>5</sup> R. C. Gonzalez and R. E. Woods, *Digital Image Processing*, Ch. 5, Addison-Wesley, Reading (1992).
- <sup>6</sup> D. R. Gerwe and P. S. Idell, "Cramér-Rao analysis of orientation estimation: viewing geometry influences on the information conveyed by target features," *Journal of the Optical Society of America A* 20, 797-816 (2003).
- <sup>7</sup> J. D. Gorman and A. O. Hero, "Lower bounds for parametric estimation with constraints," *IEEE Transactions on Information Theory* 26, 1285-1301 (1990).
- <sup>8</sup> C. C. Beckner, *Fundamental limits to noise reduction using support constraints and regularization – a Cramér-Rao bound analysis*, master's thesis, University of New Mexico (2005).
- <sup>9</sup> J. W. Goodman, *Introduction to Fourier Optics*, 3<sup>rd</sup> ed., Roberts and Company Publishers, Greenwood Village (2005).